


Momentum-selective optical absorption in triptycene molecular membraneMasashi Akita,¹ Yasumaru Fujii,² Mina Maruyama,² Susumu Okada,² and Katsunori Wakabayashi ^{1,3,4,*}¹*School of Science and Technology, Kwansei Gakuin University, Gakuen 2-1, Sanda 669-1337, Japan*²*Graduate School of Pure and Applied Science, University of Tsukuba, Tsukuba 305-8571, Japan*³*National Institute for Materials Science (NIMS), Namiki 1-1, Tsukuba 305-0044, Japan*⁴*Center for Spintronics Research Network (CSRN), Osaka University, Toyonaka 560-8531, Japan*

(Received 31 December 2019; accepted 6 February 2020; published 24 February 2020)

The optical properties of triptycene molecular membranes (TMMs) under the linearly and circularly polarized light irradiation have been theoretically studied. Since TMMs have the double-layered kagome lattice structures for their π electrons, i.e., tiling of trigonal- and hexagonal-symmetric rings, the electronic band structures of TMMs have nonequivalent Dirac cones and perfect flat bands. By constructing the tight-binding model to describe the π -electronic states of TMMs, we have evaluated the optical absorption intensities and valley selective excitation of TMMs based on the Kubo formula. It is found that absorption intensities crucially depend on both the light polarization angle and the excitation position in momentum space, i.e., the momentum and valley selective optical excitation. The polarization dependence and optical selection rules are also clarified by using group theoretical analyses.

DOI: [10.1103/PhysRevB.101.085418](https://doi.org/10.1103/PhysRevB.101.085418)**I. INTRODUCTION**

Two-dimensional (2D) atomically thin materials have attracted significant attention owing to their unique physical and chemical properties, which are derived from the low dimensionality of electronic systems [1,2]. Graphene [3] is one of the most prominent 2D materials which shows high carrier mobilities [4], half-integer quantum Hall effect [3,5], and superconductivity [6]. Owing to the honeycomb network structure of sp^2 carbon atoms [7], the electronic states of graphene near the Fermi energy are well described by using the massless Dirac equation and possess conical energy dispersion at the K and K' points of the hexagonal first Brillouin zone (BZ). These two nonequivalent Dirac K and K' points are mutually related by time-reversal symmetry. The independence and degeneracy of the valley degree of freedom owing to Dirac cones can be used to control the electronic states, i.e., valleytronics [8–12], which is analogous to spintronics and advantageous for the ultra-low-power consumption electronic devices. The idea of valleytronics is also applied to transition-metal dichalcogenide with honeycomb structure such as MoS_2 and it has been experimentally demonstrated that the electrons in each valley can be selectively excited by circularly polarized light irradiation [13–19].

Besides the hexagonal lattice structures such as graphene, the kagome lattice, which has the trihexagonal tiling network, is of interest because it also possesses an electronic energy band structure with valley structures, together with a perfect flat energy band. The kagome lattice has been the subject of intensive research and theoretical studies because of its peculiar magnetic [20–23], transport [24], and topological properties [25–30]. However, experimental fabrication

of the kagome lattice, especially composed of sp^2 carbon atoms, is considered to be difficult. Recently, the bottom-up synthesis of 2D materials has been extensively investigated. Examples of this approach are surface metal-organic frameworks (MOFs) [31] and surface covalent-organic frameworks (COFs) [32,33]. It is also suggested that the electronic states of a 2D MOF consisting of π -conjugated nickel-bis-dithiolene [34] can be modeled by the tight-binding model of a kagome lattice with the spin-orbit interactions as a candidate of topological insulators [35].

Here, we focus on the aromatic hydrocarbon triptycene [36] that is the three-dimensional (3D) propeller-type structure as the building blocks of polymerized triptycene molecular membranes (TMMs) [37,38]. There are two types of cross-linked structures in TMMs according to the bonding shape of each bridge, i.e., zigzag and armchair types. The recent first-principles calculations based on density functional theory (DFT) have shown that these TMMs are thermodynamically stable and become semiconducting with multiple kagome bands [39,40], i.e., several sets of graphene energy bands with a flat energy band. In particular, these multiple kagome bands provide a good platform of selective excitation of electrons with specific momentum, i.e., at the K and K' points.

In this paper, we theoretically study the optical properties of TMMs under the linearly and circularly polarized light irradiation. To analyze the optical properties of TMMs, we construct the tight-binding model that faithfully reproduces the energy band structure obtained by DFT, and numerically evaluate the optical absorption intensity and valley selective optical excitation using the Kubo formula [41,42]. It is found that absorption intensity crucially depends on both the light polarization angle and the momentum of optically excited electrons. It is also confirmed that the circularly polarized light irradiation can selectively excite the electrons in either

*Corresponding author: waka@kwansei.ac.jp

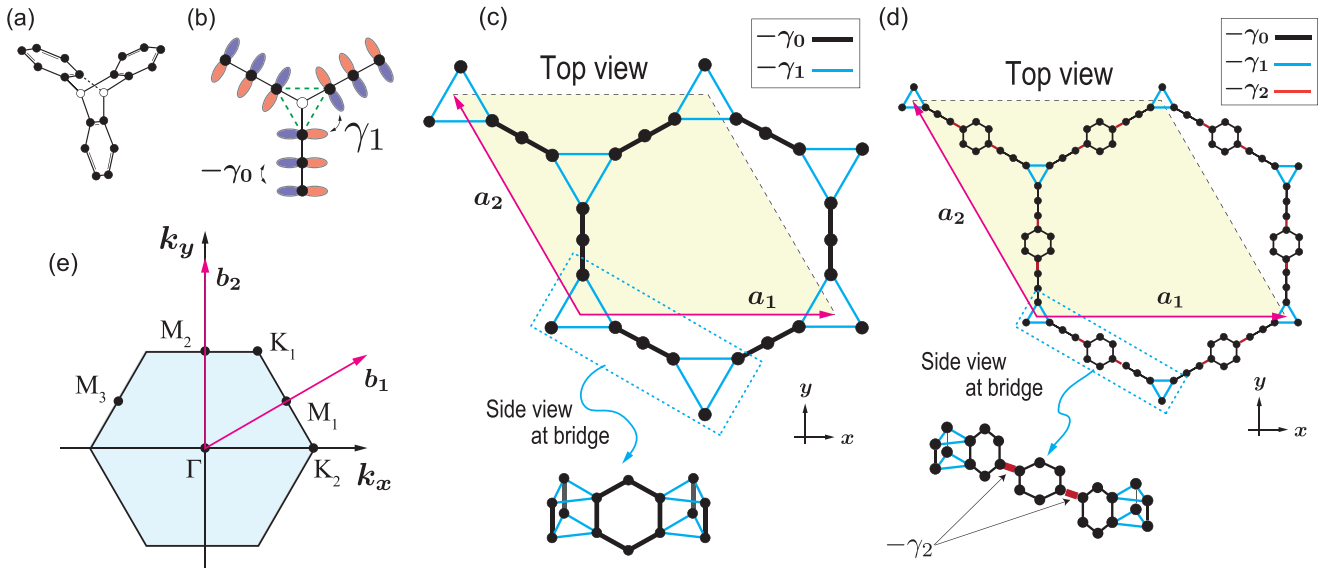


FIG. 1. (a) Schematic structure of a triptycene molecule. The black and white carbons indicate sp^2 and sp^3 carbons, respectively. Each sp^2 carbon gives one π electron. (b) Top view of the triptycene molecule together with the π orbital at each sp^2 carbon. π orbitals construct the triangle network drawn with green dashed lines. Schematic structure of (c) zigzag TMM and (d) armchair TMM. The yellow shaded rhombus indicates the unit cell of the TMMs. $\mathbf{a}_1 = (a, 0)$, $\mathbf{a}_2 = (-a/2, \sqrt{3}a/2)$ are primitive vectors, where $a = 8.92$ Å for zigzag TMM and $a = 22.17$ Å for armchair TMM, respectively. The zigzag and armchair TMMs have 18 and 54 π -electronic sites in their unit cells, respectively. (e) First BZ of TMMs.

the K or K' point. Then, we analyze the optical selection rule of TMMs using the group theory. From the analysis, we determine the selection rules of the absorption spectrum and polarization-dependent transition at the high-symmetric points in the first BZ.

This paper is organized as follows. In Sec. II, we illustrate the lattice structures of zigzag and armchair TMMs. Subsequently, we construct the tight-binding model to calculate their electronic structures and describe the fundamental theoretical framework to evaluate the optical properties of TMMs. In Sec. III, we discuss the optical properties of zigzag TMM under linearly and circularly polarized light irradiation. The optical properties of armchair TMM are discussed in Sec. IV. Section V summarizes our results. In addition, the details of the optical selection rules for a 2D kagome lattice are given in the Appendix.

II. TIGHT-BINDING MODEL OF TMM

In this paper, we employ the tight-binding model to describe the π -electronic states of TMMs and study their optical properties under the linearly and circularly polarized light irradiation. The Hamiltonian for the π orbitals in TMMs can be given as

$$\hat{H} = \sum_{(n,m)} \gamma_{n,m} |\psi_n\rangle \langle \psi_m|,$$

where ψ_m and ψ_n indicate the π orbitals at the m and n sites in the unit cell, respectively. $\gamma_{n,m}$ indicates the π -electron hopping integral between the m and n atomic sites. The detailed parametrization of $\gamma_{n,m}$ is given below.

Triptycene is the 3D aromatic molecule and is schematically shown in Fig. 1(a). The black and white circles indicate

sp^2 and sp^3 carbon atoms, respectively. Each sp^2 carbon provides one π electron. Owing to the central sp^3 carbons, three propeller wings extend toward three directions forming C_{3v} symmetry. Since there is no π electron on the center of the three propellers, the π electrons construct the triangle network in the triptycene. Figure 1(b) shows the top view of the triptycene molecule together with π orbitals. The electron hoppings within the same wing are defined as $-\gamma_0$, and those between different wings are defined as γ_1 , where $\gamma_0 > 0$ and $\gamma_1 > 0$.

As shown in Figs. 1(c) and 1(d), there are two types of cross-linked structures of TMMs, i.e., zigzag and armchair TMMs, respectively. It should be noted that both of the TMMs have C_{6v} symmetry. Here, the magenta arrows are primitive vectors, given as $\mathbf{a}_1 = (a, 0)$ and $\mathbf{a}_2 = (-\frac{a}{2}, \frac{\sqrt{3}a}{2})$, where a is the lattice constant: $a = 8.92$ Å for zigzag TMM and $a = 22.17$ Å for armchair TMM, respectively. The yellow shaded areas are the unit cells of TMMs. The zigzag and armchair TMMs have 18 and 54 π -electronic sites in their unit cells, respectively. Since the corresponding reciprocal lattice vectors are given as $\mathbf{b}_1 = \frac{2\pi}{a}(1, \frac{1}{\sqrt{3}})$ and $\mathbf{b}_2 = \frac{2\pi}{a}(0, \frac{2}{\sqrt{3}})$, the first BZ for TMMs becomes the hexagonal shown in Fig. 1(e).

In zigzag TMMs, triptycene molecules are polymerized by sharing benzene rings between neighboring molecules. It can be understood that the π electrons form the network composed of triangle rings and even membered rings as shown in Fig. 1(c). The in-plane network structure resembles the kagome lattice, where triangle- and hexagonal-symmetric rings are alternatively spread. In addition, this kagome-like network forms the bilayered structure which can be seen in the side view. The bilayer structure leads to bonding and antibonding molecular orbitals between the upper and lower layers. As shown in the Appendix, the tight-binding model of

the 2D Kagome lattice produces the energy band structures with graphene energy dispersion and a perfect flat band. In actuality, the DFT calculations show that zigzag TMMs become semiconducting and show the energy band structures accompanying several sets of kagome-like energy dispersion. For the tight-binding model of zigzag TMMs, we use $-\gamma_0$ for the electron transfer within benzene rings, and $\gamma_1 = \gamma_0/4$ for triangular rings connecting benzene rings. Throughout this paper, we set $\gamma_0 = 2.43$ eV. This parameter set fairly reproduces the energy band structures of the zigzag TMMs' obtained DFT calculations.

Figure 1(d) shows the lattice structure of armchair TMMs, where triptycene molecules are connected through benzene molecules with σ bondings. Since the benzene molecule bridges two carbon atoms belonging to the different layers as shown in the side view of the structure, armchair TMM has the rippling structure. The DFT study has shown that armchair TMM is energetically stable and semiconducting. Similar to zigzag TMM, owing to the presence of triangle rings, armchair TMMs also has kagome-like energy band structures. For the tight-binding model of armchair TMM, we use $-\gamma_0$ for the electron transfer within benzene rings, and $\gamma_1 = \gamma_0/4$ for triangular rings connecting benzene rings. It is also known that the bridging benzene rings are tilted with the angle of $\frac{\pi}{6}$ from the vertical plane to the armchair membrane owing to the conformation. Thus, the transfer integral for the bridging bonds is taken as $-\gamma_2 (= -\gamma_0 \cos \theta)$, with $\theta = \frac{\pi}{6}$. This parameter set fairly reproduces the energy band structures of the armchair TMMs' obtained DFT calculations [40].

Let us briefly give an overview of the theoretical framework used to study the optical properties of TMMs under the linearly and circularly polarized light irradiation. The light absorption coefficient of the solid is described as

$$\alpha(\omega) = \frac{\omega}{cn} \text{Im}[\varepsilon(\omega)],$$

where $\varepsilon(\omega)$ is a complex dielectric function. Here, ω is the frequency of irradiation light and n is the refractive index. In addition, the dielectric function $\varepsilon(\omega)$ can be related to the dynamical conductivity $\sigma(\omega)$ by

$$\varepsilon(\omega) = 1 + i \frac{4\pi}{\omega} \sigma(\omega).$$

Since the effect of the external field is treated within first-order perturbation, the dynamical conductivity can be evaluated through the Kubo formula [41,42], i.e.,

$$\begin{aligned} \sigma(\omega) &= \frac{\hbar}{iS} \sum_{\mathbf{k}} \sum_{i,f} \frac{f(E_{\mathbf{k}}^{(f)}) - f(E_{\mathbf{k}}^{(i)})}{E_{\mathbf{k}}^{(f)} - E_{\mathbf{k}}^{(i)}} \frac{|\mathbf{e} \cdot \langle \psi_{\mathbf{k}}^{(f)} | \nabla_{\mathbf{r}} | \psi_{\mathbf{k}}^{(i)} \rangle|^2}{E_{\mathbf{k}}^{(f)} - E_{\mathbf{k}}^{(i)} - \hbar\omega + i\eta} \\ &=: \frac{1}{S} \sum_{\mathbf{k}} \sum_{i,f} \tilde{\sigma}_{f,i}(\mathbf{k}, \omega). \end{aligned}$$

S is the area of the system and $E_{\mathbf{k}}^{(i)}$ and $E_{\mathbf{k}}^{(f)}$ indicate the eigenenergies for the initial and final states for the interband optical transition, respectively. $\psi_{\mathbf{k}}^{(i)}$ and $\psi_{\mathbf{k}}^{(f)}$ are the corresponding wave functions obtained from the tight-binding model. The \mathbf{k} summation is performed within the first BZ. $f(E_{\mathbf{k}}^{(i)})$ is the Fermi-Dirac distribution function for the state of energy $E_{\mathbf{k}}^{(i)}$. η is an infinitesimally small real number. Also,

$\mathbf{e} = (e_x, e_y)$ is the polarization vector of incident light and $\langle \psi_{\mathbf{k}}^{(f)} | \nabla_{\mathbf{r}} | \psi_{\mathbf{k}}^{(i)} \rangle$ represents the transition dipole vector, where $\nabla_{\mathbf{r}} = (\partial/\partial x, \partial/\partial y)$. For later use, we have also defined the integrand of $\sigma(\omega)$ as $\tilde{\sigma}_{f,i}(\mathbf{k}, \omega)$, which gives the momentum-resolved absorption intensity from $\psi_{\mathbf{k}}^{(i)}$ to $\psi_{\mathbf{k}}^{(f)}$, i.e., $\alpha_{f,i}(\mathbf{k}, \omega)$. This will be used for momentum-space mapping of the absorption intensity.

The transition dipole vector is evaluated as the expectation value of the group velocity [43], i.e.,

$$\langle \psi_{\mathbf{k}}^{(f)} | \nabla_{\mathbf{r}} | \psi_{\mathbf{k}}^{(i)} \rangle = i \frac{m}{\hbar} \langle \psi_{\mathbf{k}}^{(f)} | \frac{\partial \hat{H}}{\partial \mathbf{k}} | \psi_{\mathbf{k}}^{(i)} \rangle.$$

The inner product between the polarization vector and the transition dipole vector leads to

$$\begin{aligned} \mathbf{e} \cdot \langle \psi_{\mathbf{k}}^{(f)} | \nabla_{\mathbf{r}} | \psi_{\mathbf{k}}^{(i)} \rangle \\ = i \frac{m}{\hbar} \left(e_x \langle \psi_{\mathbf{k}}^{(f)} | \frac{\partial \hat{H}}{\partial k_x} | \psi_{\mathbf{k}}^{(i)} \rangle + e_y \langle \psi_{\mathbf{k}}^{(f)} | \frac{\partial \hat{H}}{\partial k_y} | \psi_{\mathbf{k}}^{(i)} \rangle \right). \end{aligned}$$

The polarization of light can be incorporated through the Jones vectors [44]. For linearly polarized light, it is given as

$$\mathbf{e}_{\text{linear}} = \begin{pmatrix} \cos \phi \\ \sin \phi \end{pmatrix},$$

where ϕ is the direction of the electric field of incident light measured from the x axis. Meanwhile, for right-handed circularly polarized (RCP) light irradiation, we use

$$\mathbf{e}_{\text{RCP}} = \frac{1}{\sqrt{2}} \begin{pmatrix} 1 \\ -i \end{pmatrix},$$

and for left-handed circularly polarized (LCP) light, we use

$$\mathbf{e}_{\text{LCP}} = \frac{1}{\sqrt{2}} \begin{pmatrix} 1 \\ i \end{pmatrix}.$$

\mathbf{e}_{RCP} and \mathbf{e}_{LCP} satisfy the orthogonality.

III. OPTICAL PROPERTIES OF ZIGZAG TMM

In this section, we consider the optical properties of zigzag TMM under linearly and circularly polarized light irradiation. Figure 2(a) shows the energy band structure of zigzag TMM together with the corresponding density of states (DOS) on the basis of the tight-binding model. The system is semiconducting with the direct band gap. Since zigzag TMM has C_{6v} symmetry that is the same as the 2D kagome lattice, several Dirac cones appear at the K point. Simultaneously, several perfect flat bands appear owing to the nature of the kagome lattice. If we assume a set of graphenelike bands with a flat band as a kagome-like energy band, as we have expected, six sets of kagome-like energy band structures are obtained. Since zigzag TMM has the bilayered structure, we can distinguish the energy subbands into bonding (black line spectrum) and antibonding (cyan line spectrum) subbands across the upper and lower layers. It is noted that optical transitions occur between the same types of states, i.e., the transition from bonding (antibonding) to antibonding (bonding) states is forbidden since the parity of the wave function is reversed with respect to the xy plane.

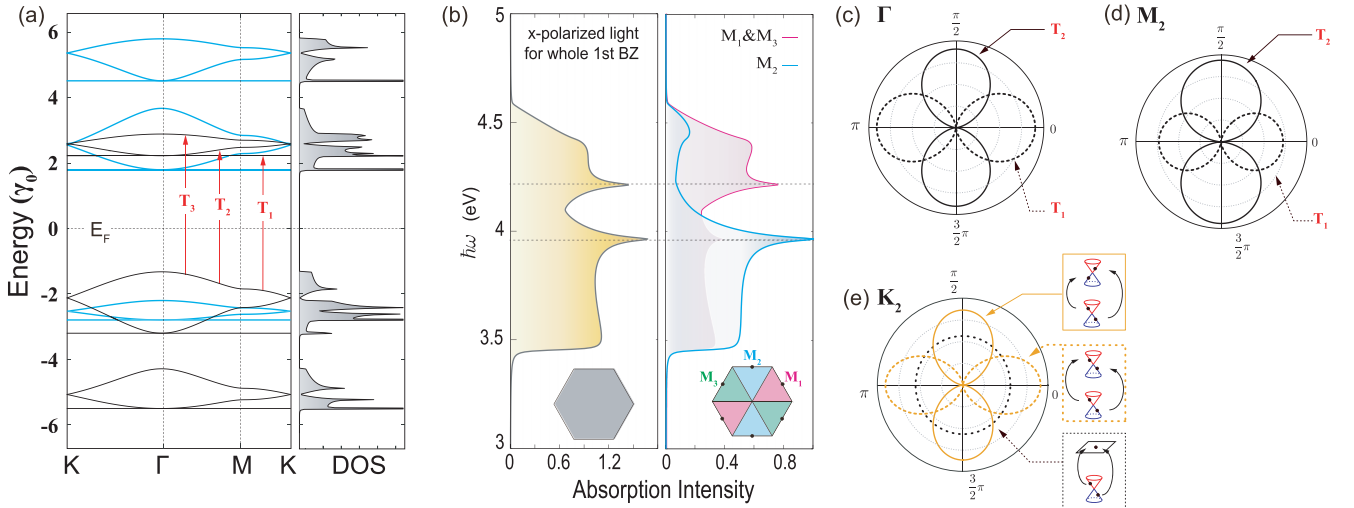


FIG. 2. (a) Energy band structure of zigzag TMM together with the corresponding DOS on the basis of the tight-binding model. Black and cyan lines in the energy band structure indicate bonding and antibonding states between the upper and lower layers, respectively. Note that the optical transition between black and cyan subbands is prohibited. The representative optical transitions from the highest valence subband are named T_1 , T_2 , and T_3 . (b) Left panel: Corresponding absorption spectrum of T_1 , T_2 , and T_3 optical transitions. The k integration is performed within the whole first BZ. Right panel: Same for T_1 , T_2 , and T_3 optical transitions, but the k integration is performed in the $1/3$ regions of the first BZ which separately contain M_1 , M_2 , and M_3 points. The angular dependence of absorption intensity at (c) Γ , (d) M_2 , and (e) K_2 points.

1. Linearly polarized light

Let us closely inspect the optical properties of zigzag TMM under linearly polarized light irradiation. To study the details of optical selection rules, we focus on the optical transition from the highest valence subband. The representative optical transitions are named T_1 , T_2 , and T_3 , indicated by red arrows in Fig. 2(a). Note that the optical transition to a cyan-colored subband is prohibited. The left panel of Fig. 2(b) shows the incident energy dependence of the absorption intensity under a linearly polarized light irradiation. Only the T_1 , T_2 , and T_3 transitions contribute optical absorption in this energy region, and k integration is performed in the whole first BZ.

The absorption spectrum shows two intensive peaks at 3.96 and 4.21 eV, which originate from the divergent joint density of states (JDOS) owing to the saddle points of the energy band structure at the M points. The first peak mainly arises from the optical transition T_1 , and the second one arises from T_2 .

It is noted that three nonequivalent M points contribute differently to these peaks of the optical absorption spectrum. The right panel of Fig. 2(b) shows the contributions from the M_1 , M_2 , and M_3 points. To separate the contribution from each M point, k integration of the optical conductivity is performed in the three divided regions, as shown in the inset of the right panel of Fig. 2(b). It is seen that the M_2 point has the larger contribution to the first peak than M_1 and M_3 , but the smaller contribution to the second peak. Thus, it is possible to make a polarization among three nonequivalent M points using the linearly polarized light irradiation.

2. Polarization angle dependence at high-symmetric k points

Next, we shall discuss the polarization angle dependence of the optical absorption intensities at the Γ , M , and K points using group theory [45]. Since the TMMs have similar crystal symmetry with the 2D kagome lattice, the polarization angle

dependence is quite analogous to the case of the 2D kagome lattice discussed in the Appendix in detail.

(1) Γ point. The Γ point has C_{6v} symmetry. However, in the kagome lattice and TMMs, the optical selection rules are determined by C_{3v} symmetry because of the existence of the triangle unit in the lattice. Thus, optical transition occurs between the nondegenerate A_1 state and the doubly degenerate E states. Therefore, only T_1 and T_2 transitions are optically active, but T_3 is prohibited.

Figure 2(c) shows the polar angle dependence of light absorption at the Γ point for T_1 and T_2 . Since the wave function of the zigzag TMM (not shown) has the same symmetry as that of the 2D kagome lattice, T_1 and T_2 have the polarization angle dependence on $\cos \phi$ and $\sin \phi$, respectively.

(2) M point. The M points have C_{2v} symmetry, i.e., there is no degeneracy in the energy dispersion at these points. In the zigzag TMM, all of the wave functions at the M points are classified into either A or B representation, similar to the case of the 2D kagome lattice. The optical transitions occur for T_1 and T_2 . It should be noted that T_3 is not allowed because T_3 connects the two states with the same symmetry. In Fig. 2(d), the angle dependence of the linearly polarized light at the M_2 point is shown. We can clearly confirm the T_1 and T_2 have $\cos \phi$ and $\sin \phi$ dependence, respectively. This is consistent with the case of the 2D kagome lattice. For the M_1 (M_3) point, the polarization angle dependence is obtained by shifting the angle as $\phi \rightarrow \phi - \pi/3$ ($\phi + \pi/3$).

(3) K point. The K points have C_{3v} symmetry. Similar to the 2D kagome lattice, nondegenerate A_1 states and doubly degenerate E states appear at the K points in zigzag TMM. The flat band state corresponds to A_1 , and the Dirac points correspond to E states. Thus, the optical transitions are allowed between A_1 and E states, i.e., T_1 , and between E states, i.e., T_2 and T_3 . However, it is noted that the optical absorption is relatively

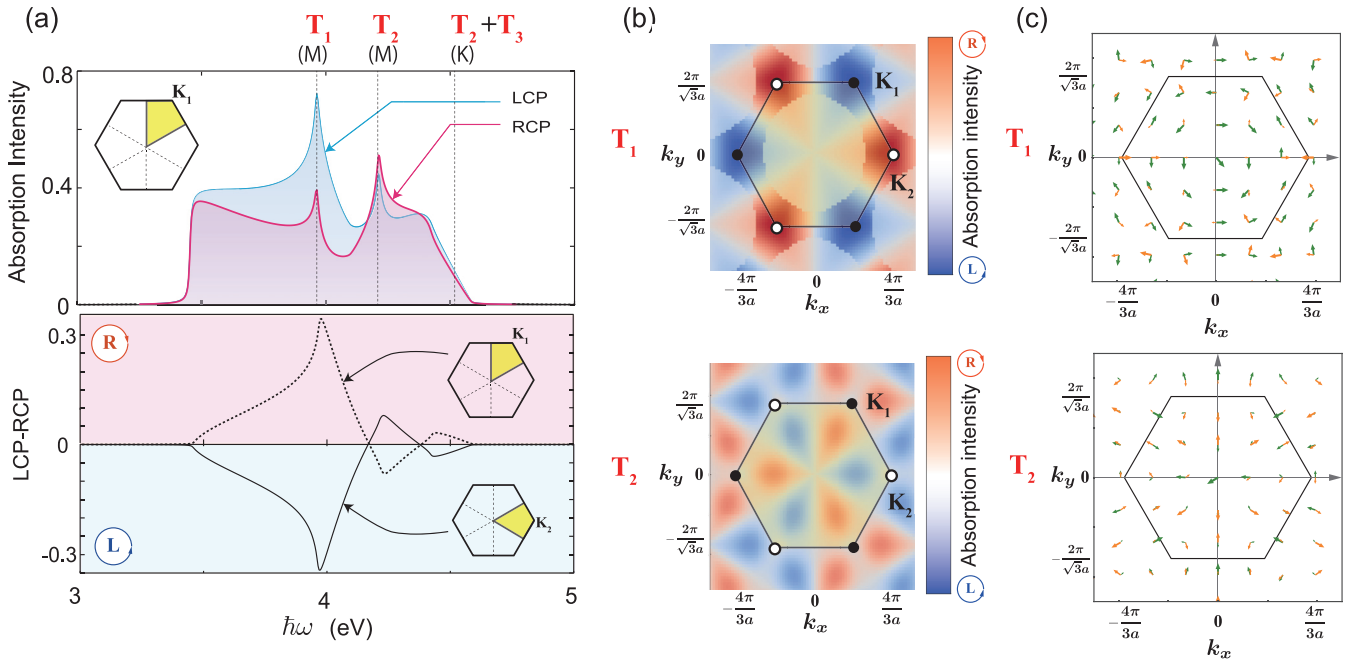


FIG. 3. (a) Upper panel: Optical absorption spectrum of zigzag TMM under the circularly polarized light irradiation. The three dashed lines indicate the representative optical transition caused by T_1 at the M point, T_2 at the M point, and $T_2 + T_3$ at the K point, from the left. The integration is evaluated within the $1/6$ region of the first BZ containing the K_2 point. Lower panel: The difference of optical absorption between LCP and RCP. The dashed and solid lines correspond to the cases of k integration for the $1/6$ regions of the BZ containing K_1 and K_2 , respectively. Since TMM preserves both time-reversal and inversion symmetries, the K_1 and K_2 states polarize oppositely, i.e., no net valley polarization. (b) Momentum-space mapping of the absorption intensity difference between LCP and RCP, i.e., $\Delta\alpha(\mathbf{k})$ for T_1 (upper panel) and T_2 (lower panel) transitions. (c) The distribution of the dipole vector in the momentum space for T_1 (upper panel) and T_2 (lower panel) transitions under the circularly polarized light irradiation. The green and orange arrows indicate the real and imaginary parts of the dipole vector, respectively.

weak compared with those at the Γ and M points, owing to the smaller JDOS of Dirac cones in zigzag TMM.

The angle dependence at the K points is shown in Fig. 2(e). It is noted that the optical transition of T_1 is isotropic, which is not seen in the Γ and M points. It is equivalent to the polarization dependence of the 2D kagome lattice; see the Appendix.

Furthermore, in TMMs, the unique optical transitions occur between Dirac cones, which are absent in the simple 2D kagome lattice. Similar to graphene, the Dirac cones are expected to have the helicity. In general, the upper and lower cones have opposite helicities even at the same K point. The red and blue Dirac cones in Fig. 2(e) indicate the opposite helicity. It should be noted that the optical transitions between the same (different) helicities have the polarization angle dependence of $\sin\phi$ ($\cos\phi$). Thus, the polarization dependence of the absorption spectrum at the K points has a different origin from those at the Γ and M points.

3. Circularly polarized light

Since zigzag TMM has the valley structures in the energy band structure, the circularly polarized light irradiation can selectively excite the electrons belonging to either the K_1 or K_2 point, depending on the direction of the polarization. Note that the present system preserves both time-reversal and inversion symmetries, and no net valley polarization occurs. The upper panel of Fig. 3(a) is the absorption spectrum

under the circularly polarized light irradiation, where the k integration has been performed within the $1/6$ region of the BZ containing the K_2 point; see the inset of Fig. 3(a). It can be noticed that there are two pronounced peaks around $\hbar\omega = 3.96$ and 4.21 eV, where only the first peak shows a rather large difference between LCP and RCP. The first and second peaks correspond to the optical transition of T_1 and T_2 at the M point, respectively. The optical transition of T_1 is mainly dominated by the electronic excitation at the M and K points. However, T_2 is mostly dominated by electronic excitation at the M points. The lower panel of Fig. 3(a) is the difference of the optical absorption between LCP and RCP. Since TMM preserves both time-reversal and inversion symmetries, the K_1 and K_2 states polarize oppositely, i.e., no net valley polarization.

Figure 3(b) shows momentum-space mappings of the absorption intensity differences between LCP and RCP, $\Delta\alpha(\mathbf{k})$, for the optical transitions T_1 and T_2 . $\Delta\alpha(\mathbf{k})$ is defined as $\Delta\alpha(\mathbf{k}) := \alpha_{(f,i)}^{\text{LCP}}(\mathbf{k}, \omega) - \alpha_{(f,i)}^{\text{RCP}}(\mathbf{k}, \omega)$, where (f, i) and ω are chosen to satisfy the condition of specific optical transition. The red (blue) region indicates strong absorption for RCP (LCP). The strong valley selective excitation by circularly polarized light irradiation can be observed for the optical transition T_1 . However, such valley selective excitation becomes weak for T_2 . This can be understood by inspecting the momentum-space mapping of the dipole vector, $\langle \psi_{\mathbf{k}}^{(f)} | \nabla_r | \psi_{\mathbf{k}}^{(i)} \rangle$, as shown in Fig. 3(c), where the green and orange arrows indicate the real and imaginary parts of the dipole

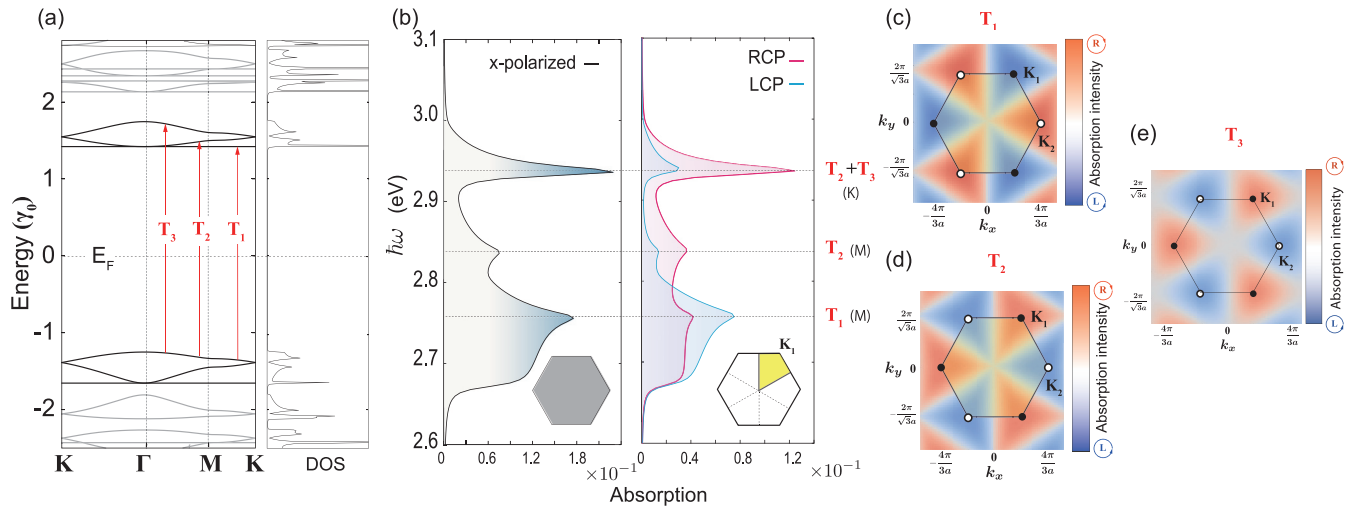


FIG. 4. (a) Energy band structure of armchair TMM together with DOS on the basis of the tight-binding model. The optical transitions from the highest valence subband to the lowest three conduction subbands are named T_1 , T_2 , and T_3 . (b) Optical absorption spectrum of armchair TMM under linear (left panel) and circular (right panel) irradiation. For linear irradiation, k integration is performed for the whole first BZ. There are three pronounced peaks at $\hbar\omega = 2.76$, 2.84 , and 2.94 eV. At the right side of the panel, the dominant optical transition and the high-symmetric points where the optical transitions occur are noted. For circular irradiation, k integration is performed for the $1/6$ region of the first BZ containing K_1 . (c)–(e) Momentum-space mapping of the absorption intensity difference between RCP and LCP, i.e., $\Delta\alpha(\mathbf{k})$ for (c) T_1 , (d) T_2 , and (e) T_3 transitions.

vector, respectively. As can be seen, the real and imaginary parts are orthogonal near the K_1 and K_2 points for T_1 , resulting in the valley selective excitation [46,47]. However, the real and imaginary parts of the dipole vector becomes parallel in the transition T_2 , i.e., very weak valley selective excitation. Note that the momentum mapping of absorption intensity for T_3 is not shown here because T_3 is optically prohibited except in the vicinity of K points.

IV. OPTICAL PROPERTIES OF ARMCHAIR TMM

In this section, we briefly discuss the optical properties of armchair TMM. For armchair TMM, we can apply similar optical selection rules as found in zigzag TMM. However, owing to the less dispersive energy band structures of armchair TMM, rather clear valley selective optical excitation can be observed.

Figure 4(a) shows the energy band structure of armchair TMM together with the corresponding DOS on the basis of the tight-binding model. Here the tilted angle is set to $\frac{\pi}{6}$. Similarly, several sets of kagome bands are obtained. Since the unit cell contains 54 atomic sites, only subbands and DOS near the Fermi energy are shown. Owing to the rippling structure of armchair TMMs, we cannot decompose the energy subbands into bonding and antibonding states. Similar to the case of zigzag TMM, let us focus on the optical transition from the highest valence subband to the three lowest conduction subbands indicated as T_1 , T_2 , and T_3 in Fig. 4(a). Note that no valley polarization occurs because both time-reversal and inversion symmetries are preserved.

In armchair TMM, the absorption spectrum of these transitions has the two strong peaks around 2.76 and 2.94 eV, in addition to one weak peak around the 2.84 eV, as shown in the left panel of Fig. 4(b). Here, k integration is performed in the whole first BZ. The first strong peak and second weak peak

indicate the T_1 and T_2 transitions at the M point, respectively. However, the third strong peak indicates the T_2 and T_3 transitions at the K point. In armchair TMM, the slope of the energy dispersion for Dirac cones becomes smaller than that of zigzag TMM, leading to a faster increase of DOS near the Dirac points. This fact induces rather strong valley selective optical absorption at the K point for $\hbar\omega = 2.94$ eV. Thus, armchair TMM can generate the valley selective optical excitation more clearly, as shown in the right panel of Fig. 4(b). Here, k integration is performed in the $1/6$ region of the first BZ containing the K_1 point; see the inset of Fig. 4(b). Certainly, the momentum-space mappings of the absorption spectrum differences $\Delta\alpha(\mathbf{k})$ for the T_1 , T_2 , and T_3 transitions clearly indicate the selective excitation around the K_1 and K_2 points, as shown in Figs. 4(c)–4(e).

V. SUMMARY

In summary, we have theoretically investigated the optical properties of TMMs under the linearly and circularly polarized light irradiation. To analyze the optical properties of TMMs, we have constructed the tight-binding model that faithfully reproduces the energy band structures obtained by first-principles calculations. On the basis of the tight-binding model, we have numerically evaluated the optical absorption intensity and valley selective optical excitation using the Kubo formula. This approach significantly reduces the computational cost since the TMMs contain the large number of atoms in their unit cells. It is found that absorption intensity crucially depends on both the light polarization angle and the momentum of optically excited electrons. It has also been confirmed that the circularly polarized light irradiation can selectively excite the electrons in either the K or K' point. Besides the circularly polarized light irradiation, the use of second optical harmonics [48] is another way to generate the

valley polarization in TMMs, which will be studied in the future. Thus, TMMs are considered to be a good platform for valleytronics applications. In addition, we have analyzed the selection rules of TMMs using group theory, which shows very similar optical selection rules to that of the 2D kagome lattice system. From the analysis, we have determined the absorption spectrum and polarization-dependent transition at high-symmetric points in the first BZ. Our work will serve to design further TMMs and analyze the experimental data of the optical absorption spectrum of TMMs.

ACKNOWLEDGMENTS

K.W. acknowledges the financial support from the Masuya Memorial Research Foundation of Fundamental Research. This work was supported by JSPS KAKENHI Grant No. JP18H01154, and JST CREST Grant No. JPMJCR19T1.

APPENDIX: SELECTION RULE OF 2D KAGOME LATTICE

Here we consider the electronic states of the 2D kagome lattice and summarize the optical selection rules on the basis of the nearest-neighbor tight-binding model. Figure 5(a) shows a schematic of the 2D kagome lattice. The yellow shaded area is the unit cell, which contains three nonequivalent atomic sites called A , B , and C . The primitive vectors are given as $\mathbf{a}_1 = (a, 0)$ and $\mathbf{a}_2 = (-\frac{a}{2}, \frac{\sqrt{3}a}{2})$, where a is the lattice constant. Here, we assume that each site has a single electronic orbital, and the electron hopping parameter between nearest-neighbor sites is $-\gamma$.

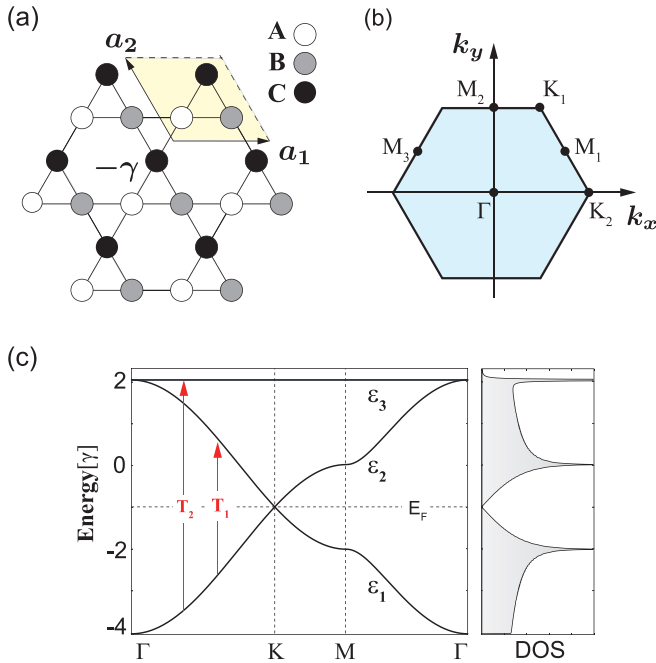


FIG. 5. (a) Schematic of the 2D kagome lattice. The yellow area represents the unit cell and the primitive vectors are $\mathbf{a}_1 = (a, 0)$, $\mathbf{a}_2 = (-\frac{a}{2}, \frac{\sqrt{3}a}{2})$. $-\gamma$ is the hopping parameter between the nearest-neighbor sites. (b) First BZ. (c) Energy band structure and DOS. The optical transition from ϵ_1 to ϵ_2 (ϵ_3) is defined as T_1 (T_2).

TABLE I. Character table of C_{6v} .

C_{6v}	E	$2C_6(z)$	$2C_3(z)$	$C_2(z)$	$3\sigma_v$	$3\sigma_d$	
A_1	1	1	1	1	1	1	z
A_2	1	1	1	1	-1	-1	
B_1	1	-1	1	-1	1	-1	
B_2	1	-1	1	-1	-1	1	
E_1	2	1	-1	-2	0	0	(x, y)
E_2	2	-1	-1	2	0	0	

The Schrödinger equation for the 2D kagome lattice is given as

$$\hat{H}_k \psi_k = \epsilon_k \psi_k,$$

where $\psi_k = (A_k, B_k, C_k)$ is the wave function representing the amplitude at the A , B , and C sublattice sites in the unit cell, respectively. ϵ_k is the energy eigenvalue. The Hamiltonian is given by

$$\hat{H}_k = -\gamma \begin{pmatrix} 0 & 1 + e^{iK_1} & 1 + e^{-iK_3} \\ 1 + e^{-iK_1} & 0 & 1 + e^{iK_2} \\ 1 + e^{iK_3} & 1 + e^{-iK_2} & 0 \end{pmatrix}.$$

Here, we have defined $K_v = \mathbf{k} \cdot \mathbf{a}_v / 2$, with $v = (1, 2, 3)$, $\mathbf{k} = (k_x, k_y)$, and $\mathbf{a}_3 = -(\mathbf{a}_1 + \mathbf{a}_2)$. Since the reciprocal lattice vectors are given as $\mathbf{b}_1 = \frac{2\pi}{a}(1, \frac{1}{\sqrt{3}})$ and $\mathbf{b}_2 = \frac{2\pi}{a}(0, \frac{2}{\sqrt{3}})$, the first BZ of the 2D Kagome lattice becomes hexagonal, as shown in Fig. 5(b). The energy eigenvalues are given as $\epsilon_k / \gamma = 2, -1 \pm \sqrt{3 + 2 \sum_{v=1}^3 \cos(K_v)}$. It should be noted that the form $\pm \sqrt{3 + 2 \sum_{v=1}^3 \cos(K_v)}$ is completely identical to the form of energy band dispersion of the nearest-neighbor tight binding model for π electrons of graphene.

Figure 5(c) shows the energy band structure and corresponding density of states of the 2D kagome lattice. There are three subbands in this system, and the two lowest subbands have an identical structure to that of a 2D honeycomb lattice, i.e., graphene. However, there is the perfect flat band over the first BZ at $\epsilon = 2\gamma$. Hereafter, we call the energy subband ϵ_1 , ϵ_2 , and ϵ_3 from the lowest one to the highest one, and the corresponding wave functions ψ_1 , ψ_2 , and ψ_3 , respectively. We also define the optical transition from ϵ_1 to ϵ_2 (ϵ_3) as T_1 (T_2).

Let us discuss the optical selection rules and polarization angle dependence of the 2D kagome lattice at high-symmetric \mathbf{k} points, i.e., $\Gamma = (0, 0)$, $K_2 = \frac{2\pi}{a}(\frac{2}{3}, 0)$, and $M_1 = \frac{2\pi}{a}(0, \frac{1}{\sqrt{3}})$.

(1) Γ point. The Γ point has C_{6v} symmetry, which obeys the character table of Table I. At the Γ point, the eigenenergies are $\epsilon_1 = -4\gamma$, and $\epsilon_2 = \epsilon_3 = 2\gamma$. The wave function is analytically given as

$$\begin{aligned} \langle \psi_1^\Gamma | &= \frac{1}{\sqrt{3}}(1, 1, 1), & \langle \psi_2^\Gamma | &= \sqrt{\frac{2}{3}}\left(-\frac{1}{2}, -\frac{1}{2}, 1\right), \\ \langle \psi_3^\Gamma | &= \frac{1}{\sqrt{2}}(1, -1, 0), \end{aligned}$$

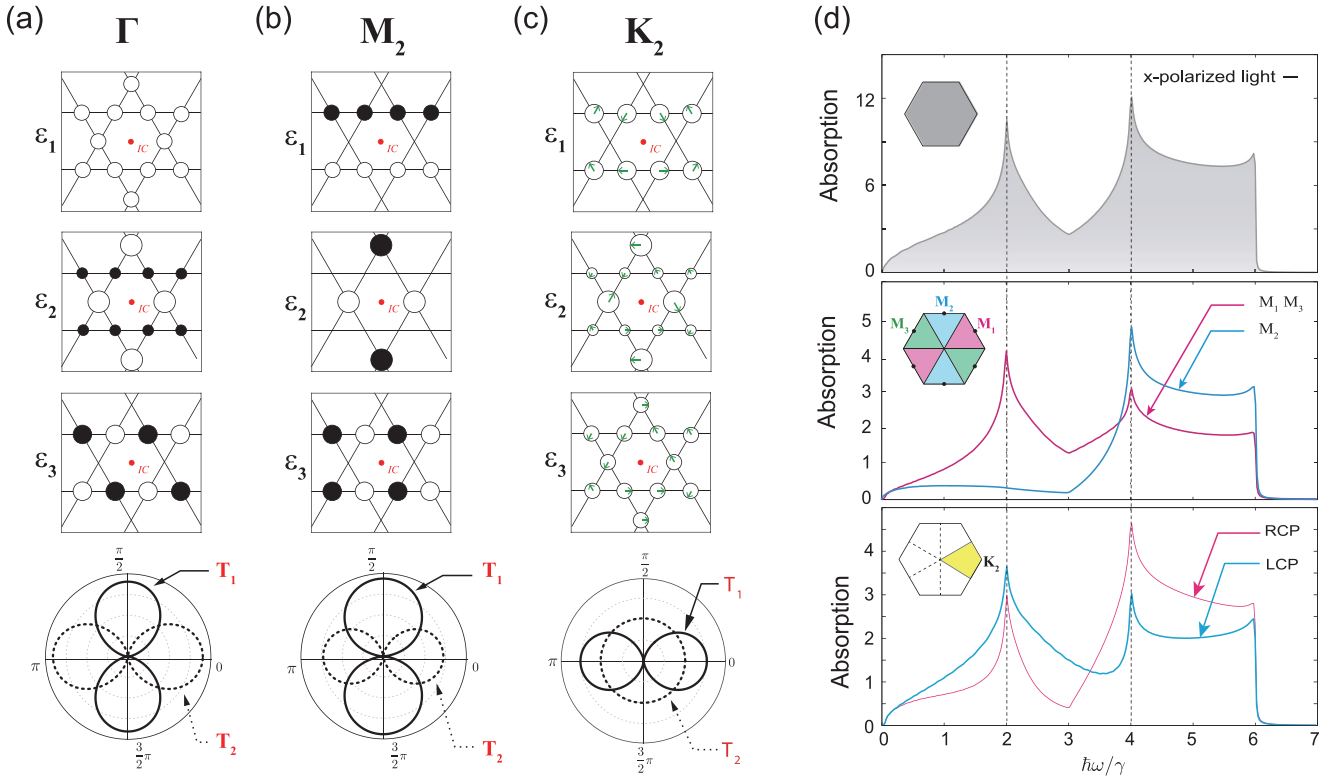


FIG. 6. The real-space distribution of wave functions for the 2D Kagome lattice and corresponding angle dependence (bottom panel) of optical absorption at high-symmetric points: (a) Γ and (b) M_2 . Black and white circles indicate the sign of the wave functions, and the radius of the circles indicates the amplitude of the wave functions. Red dots indicate the inversion center (IC) of the kagome lattice. (c) Same for the K_2 point. Here, the argument of complex wave function is indicated by green arrows. (d) Absorption intensity and polarization of the 2D kagome lattice, where k integration for optical conductivity is performed (upper panel) for the whole first BZ (upper panel), for 1/3 regions of the first BZ containing either the M_1 , M_2 or M_3 point (middle panel), and for the 1/6 region of the first BZ containing the K_2 point (lower panel).

which are schematically drawn in Fig 6(a). According to the character table of C_{6v} , ψ_1 is A_1 representation, and the degenerate states of ψ_2 and ψ_3 are E_2 representation. Since the polarization vectors belong to E_1 representation, the tensor product $E_1 \otimes A_1 = E_1$ indicates that the optical transition to E_2 is not allowed. However, it should be noted that the 2D Kagome lattice contains C_{3v} symmetry if we take the triangle unit as the symmetry center. According to the character table of C_{3v} (see Table II), ψ_1 is A_1 representation, and the degenerate states of ψ_2 and ψ_3 are E representation. Since in C_{3v} the tensor product is given as $E \otimes A_1 = E$, both of the optical transitions T_1 and T_2 are active. Furthermore, the basis functions for the ψ_1 , ψ_2 , and ψ_3 states are given as z , y , and x , respectively. The optical transitions T_1 and T_2 have x and y polarization, respectively.

Since the wave functions are analytically obtained, we can analytically evaluate the expectation values of the optical

dipole vectors. For linear polarization, we obtain

$$\begin{aligned} \mathbf{e} \cdot \langle \psi_2 | \nabla_k H | \psi_1 \rangle &= -i \frac{3\sqrt{3}a}{2\sqrt{2}} \sin \phi, \\ \mathbf{e} \cdot \langle \psi_3 | \nabla_k H | \psi_1 \rangle &= i \frac{3a}{\sqrt{6}} \cos \phi. \end{aligned}$$

This polarization angle dependence is consistent with the numerical calculations, as shown in the bottom panel of Fig. 6(a). For circular polarization, we obtain

$$|\mathbf{e}_{\text{LCP}} \cdot \langle \psi_j | \nabla_k H | \psi_1 \rangle|^2 = |\mathbf{e}_{\text{RCP}} \cdot \langle \psi_j | \nabla_k H | \psi_1 \rangle|^2,$$

where $j = 2, 3$. Thus, there is no dependence on the direction of circular polarization at the Γ point.

(2) M point. The M points have C_{2v} symmetry, which obeys the character table of Table III. The eigenenergies are

TABLE II. Character table of C_{3v} .

C_{3v}	E	$2C_3(z)$	$3\sigma_v$	
A_1	1	1	1	z
A_2	1	1	-1	
E	2	-1	0	(x, y)

TABLE III. Character table of C_{2v} .

C_{2v}	E	C_2	$\sigma_v(xz)$	$\sigma_v(yz)$	
A_1	1	1	1	1	z
A_2	1	1	-1	-1	
B_1	1	-1	1	-1	x
B_2	1	-1	-1	1	y

$\epsilon_1 = -2\gamma$, $\epsilon_2 = 0$, and $\epsilon_3 = 2\gamma$, respectively. For example, the wave functions at the M_2 point are given as

$$\begin{aligned} \langle \psi_1^{M_2} | &= \frac{1}{\sqrt{2}}(1, 1, 0), & \langle \psi_2^{M_2} | &= (0, 0, 1), \\ \langle \psi_3^{M_2} | &= \frac{1}{\sqrt{2}}(1, -1, 0), \end{aligned}$$

which are schematically shown in Fig. 6(b). Since C_{2v} is a 1D representation, we can define two symmetry axes in real space. $\psi_1^{M_2}$, $\psi_2^{M_2}$, and $\psi_3^{M_2}$ along the x (y) direction are A_1 , A_1 , and B_1 (B_2, A_1 , and A_1) representations, respectively. Note that the basis functions for B_1 and B_2 are x and y , respectively. Thus, optical transition T_1 (T_2) is active with y (x) polarization. For linear polarization, we can explicitly write the expectation value of the dipole vector as

$$\begin{aligned} \mathbf{e} \cdot \langle \psi_2^{M_2} | \nabla_k H | \psi_1^{M_2} \rangle &= -i\sqrt{\frac{3}{2}} \sin \phi, \\ \mathbf{e} \cdot \langle \psi_3^{M_2} | \nabla_k H | \psi_1^{M_2} \rangle &= -i \cos \phi. \end{aligned}$$

The M_2 point has mirror with respect to the k_y axis; however, M_1 and M_3 have the mirror with respect to $k_y = \frac{1}{\sqrt{3}}k_x$ and $k_y = -\frac{1}{\sqrt{3}}k_x$, respectively. Thus, the polarization angle dependence for M_1 and M_3 can be obtained by replacing the result of M_2 as $\phi \rightarrow \phi - \pi/3$ and $\phi \rightarrow \phi + \pi/3$, respectively. Thus, by tuning the angle of linear polarization, the electrons can be optically excited either by the M_1 , M_2 , or M_3 point selectively.

(3) K_2 point. The K_1 and K_2 points have C_{3v} symmetry. The eigenenergies are $\epsilon_1 = \epsilon_2 = -\gamma$ and $\epsilon_3 = 2\gamma$. The wave function at the K_2 point is given as

$$\begin{aligned} \langle \psi_1^{K_2} | &= \frac{1}{\sqrt{2}}(-\omega^{-1}, 0, 1)^*, & \langle \psi_2^{K_2} | &= \frac{1}{\sqrt{2}}(1 - 2\omega, 2, -\omega^{-1})^*, \\ \langle \psi_3^{K_2} | &= \frac{1}{\sqrt{3}}(\omega^{-1}, \omega, 1)^*, \end{aligned}$$

where $\omega = \exp(i\frac{2\pi}{3})$. ψ_3 has A_1 representation, and the degenerate states of ψ_1 and ψ_2 have E representation. For the degenerate ψ_1 and ψ_2 states, we made the orthonormalization. Since the tensor product leads to $E \otimes E = A_1$, the optical transition from the Dirac cone to the flat band is active.

For linear polarization, we can explicitly write the expectation value of the dipole vector as

$$\begin{aligned} \mathbf{e} \cdot \langle \psi_3^{K_2} | \nabla_k H | \psi_1^{K_2} \rangle &= -i\frac{\sqrt{3}}{2\sqrt{2}}\omega^{-1} \exp(i\phi), \\ \mathbf{e} \cdot \langle \psi_3^{K_2} | \nabla_k H | \psi_2^{K_2} \rangle &= \frac{\sqrt{3}}{2\sqrt{2}}\omega^{-1} \exp(-i\phi). \end{aligned}$$

The polarization angle works only for the phase factor, i.e., no polarization angle dependence. This behavior is shown in the bottom panel of Fig. 6(c). For circularly polarized light, the expectation values of the dipole vector are written as

$$\begin{aligned} \mathbf{e}_{\text{RCP}} \cdot \langle \psi_3^{K_2} | \nabla_k H | \psi_1^{K_2} \rangle &= -i\frac{\sqrt{3}}{\sqrt{2}}\omega^{-1}, \\ \mathbf{e}_{\text{LCP}} \cdot \langle \psi_3^{K_2} | \nabla_k H | \psi_1^{K_2} \rangle &= 0, \\ \mathbf{e}_{\text{RCP}} \cdot \langle \psi_3^{K_2} | \nabla_k H | \psi_2^{K_2} \rangle &= \frac{\sqrt{3}}{\sqrt{2}}\omega^{-1}, \\ \mathbf{e}_{\text{LCP}} \cdot \langle \psi_3^{K_2} | \nabla_k H | \psi_2^{K_2} \rangle &= 0. \end{aligned}$$

Thus, only RCP light can excite electrons at the K_1 points, i.e., *valley selective optical excitation*. On the contrary, at the K_2 points, only LCP light can excite electrons. However, it is noted that the optical absorption is relatively weak compared with those at the Γ and M points, owing to the smaller JDOS of the Dirac cones.

Absorption intensity. Figure 6(d) shows the energy dependence of the absorption intensity for the linearly and circularly polarized light irradiation, together with the valley selective optical excitation. In the upper panel of Fig. 6(d), the spectrum is integrated over the whole first BZ, and the sharp peaks at $\hbar\omega = 2\gamma$ and 4γ are originated from optical transition at the M point, where JDOS diverges logarithmically.

It is intriguing that the lower peak at 2γ is dominated by the optical transition T_1 , as shown in middle panel of Fig. 6(d). This behavior is attributed to the angle dependence at the M point shown in Fig. 6(b). Thus, the lower peak has strong momentum selectivity for the optical absorption. For the higher peak at 4γ , no such strong selectivity is found. Also, for circularly polarized light irradiation, such strong polarization dependence does not occur, as shown in the lower panel of Fig. 6(d). Instead, the valley selective optical excitation is relatively enhanced around $\hbar\omega = 3\gamma$. Around this energy, optical transition occurs mainly at the K points between the Dirac cones and flat band. Although the optical absorption intensity is not so large owing to the relatively small DOS near the Dirac cones, they show stronger valley selective optical excitation.

- [1] M. Chhowalla, H. Shin, G. Eda, L. Li, K. Loh, and H. Zhang, *Nat. Chem.* **5**, 263 (2013).
 [2] S. Z. Butler, S. M. Hollen, L. Cao, Y. Cui, J. A. Gupta, H. R. Guti'erez, T. F. Heinz, S. S. Hong, J. Huang, A. F. Ismach, E. Johnston-Halperin, M. Kuno, V. V. Plashnitsa, R. D. Robinson, R. S. Ruoff, S. Salahuddin, J. Shan, L. Shi, M. G. Spencer,

- M. Terrones, W. Windl, and J. E. Goldberger, *ACS Nano* **7**, 2898 (2013).
 [3] K. S. Novoselov, A. K. Geim, S. V. Morozov, D. Jiang, M. I. Katsnelson, I. V. Grigorieva, S. V. Dubonos, and A. A. Firsov, *Nature (London)* **438**, 197 (2005).

- [4] C. R. Dean, A. F. Young, I. Meric, C. Lee, L. Wang, S. Sorgenfrei, K. Watanabe, T. Taniguchi, P. Kim, K. L. Shepard, and J. Hone, *Nat. Nanotechnol.* **5**, 722 (2010).
- [5] Y. Zhang, Y.-W. Tan, H. L. Stormer, and P. Kim, *Nature (London)* **438**, 201 (2005).
- [6] Y. Cao, V. Fatemi, S. Fang, K. Watanabe, T. Taniguchi, E. Kaxiras, and P. Jarillo-Herrero, *Nature (London)* **556**, 43 (2018).
- [7] A. H. Castro Neto, F. Guinea, N. M. R. Peres, K. S. Novoselov, and A. K. Geim, *Rev. Mod. Phys.* **81**, 109 (2009).
- [8] J. R. Schaibley, H. Yu, G. Clark, P. Rivera, J. S. Ross, K. L. Seyler, W. Yao, and X. Xu, *Nat. Rev. Mater.* **1**, 16055 (2016).
- [9] A. Rycerz, J. Tworzydło, and C. W. J. Beenakker, *Nat. Phys.* **3**, 172 (2007).
- [10] D. Xiao, W. Yao, and Q. Niu, *Phys. Rev. Lett.* **99**, 236809 (2007).
- [11] D. Gunlycke and C. T. White, *Phys. Rev. Lett.* **106**, 136806 (2011).
- [12] L. E. Golub, S. A. Tarasenko, M. V. Entin, and L. I. Magarill, *Phys. Rev. B* **84**, 195408 (2011).
- [13] K. F. Mak, K. L. McGill, J. Park, and P. L. McEuen, *Science* **344**, 1489 (2014).
- [14] Q. H. Wang, K. Kalantar-Zadeh, A. Kis, J. N. Coleman, and M. S. Strano, *Nat. Nanotechnol.* **7**, 699 (2012).
- [15] D. Xiao, G.-B. Liu, W. Feng, X. Xu, and W. Yao, *Phys. Rev. Lett.* **108**, 196802 (2012).
- [16] H. Zeng, J. Dai, W. Yao, D. Xiao, and X. Cui, *Nat. Nanotechnol.* **7**, 490 (2012).
- [17] G. Kioseoglou, A. Hanbicki, M. Currie, A. Friedman, D. Gunlycke, and B. Jonker, *Appl. Phys. Lett.* **101**, 221907 (2012).
- [18] G. Sallen, L. Bouet, X. Marie, G. Wang, C. R. Zhu, W. P. Han, Y. Lu, P. H. Tan, T. Amand, B. L. Liu, and B. Urbaszek, *Phys. Rev. B* **86**, 081301(R) (2012).
- [19] S. Wu, C. Huang, G. Aivazian, J. S. Ross, D. H. Cobden, and X. Xu, *ACS Nano* **7**, 2768 (2013).
- [20] A. Mielke, *J. Phys. A: Math. Gen.* **25**, 4335 (1999).
- [21] J. S. Helton, K. Matan, M. P. Shores, E. A. Nytko, B. M. Bartlett, Y. Yoshida, Y. Takano, A. Suslov, Y. Qiu, J.-H. Chung, D. G. Nocera, and Y. S. Lee, *Phys. Rev. Lett.* **98**, 107204 (2007).
- [22] S. Yan, D. Huse, and S. White, *Science (NY)* **332**, 1173 (2011).
- [23] S. Sachdev, *Phys. Rev. B* **45**, 12377 (1992).
- [24] G. Liu, S.-L. Zhu, S. Jiang, F. Sun, and W. M. Liu, *Phys. Rev. A* **82**, 053605 (2010).
- [25] G. Liu, P. Zhang, Z. Wang, and S.-S. Li, *Phys. Rev. B* **79**, 035323 (2009).
- [26] H.-M. Guo and M. Franz, *Phys. Rev. B* **80**, 113102 (2009).
- [27] Y. Hatsugai and I. Maruyama, *Europhys. Lett.* **95**, 20003 (2011).
- [28] W. Beugeling, J. C. Everts, and C. Morais Smith, *Phys. Rev. B* **86**, 195129 (2012).
- [29] M. Ezawa, *Phys. Rev. Lett.* **120**, 026801 (2018).
- [30] A. Bolens and N. Nagaosa, *Phys. Rev. B* **99**, 165141 (2019).
- [31] R. Makiura, S. Motoyama, Y. Umemura, H. Yamanaka, O. Sakata, and H. Kitagawa, *Nat. Mater.* **9**, 565 (2010).
- [32] J. W. Colson, A. R. Woll, A. Mukherjee, M. P. Levendorf, E. L. Spitzer, V. B. Shields, M. G. Spencer, J. Park, and W. R. Dichtel, *Science* **332**, 228 (2011).
- [33] E. L. Spitzer, B. T. Koo, J. L. Novotney, J. W. Colson, F. J. Uribe-Romo, G. D. Gutierrez, P. Clancy, and W. R. Dichtel, *J. Am. Chem. Soc.* **133**, 19416 (2011).
- [34] T. Kambe, R. Sakamoto, K. Hoshiko, K. Takada, M. Miyachi, J.-H. Ryu, S. Sasaki, J. Kim, K. Nakazato, M. Takata, and H. Nishihara, *J. Am. Chem. Soc.* **135**, 2462 (2013).
- [35] Z. F. Wang, N. Su, and F. Liu, *Nano Lett.* **13**, 2842 (2013).
- [36] P. D. Bartlett, M. J. Ryan, and S. G. Cohen, *J. Am. Chem. Soc.* **64**, 2649 (1942).
- [37] C. Zhang, Y. Liu, B. Li, B. Tan, C.-F. Chen, H.-B. Xu, and X.-L. Yang, *ACS Macro Lett.* **1**, 190 (2012).
- [38] R. Bhola, P. Payamyar, D. J. Murray, B. Kumar, A. J. Teator, M. U. Schmidt, S. M. Hammer, A. Saha, J. Sakamoto, A. D. Schlüter, and B. T. King, *J. Am. Chem. Soc.* **135**, 14134 (2013).
- [39] Y. Fujii, M. Maruyama, K. Wakabayashi, K. Nakada, and S. Okada, *J. Phys. Soc. Jpn.* **87**, 034704 (2018).
- [40] Y. Fujii, M. Maruyama, and S. Okada, *Jpn. J. Appl. Phys.* **57**, 125203 (2018).
- [41] R. Kubo, *J. Phys. Soc. Jpn.* **12**, 570 (1957).
- [42] G. D. Mahan, *Many-Particle Physics* (Springer, New York, 2000).
- [43] L. C. Lew Yan Voon and L. R. Ram-Mohan, *Phys. Rev. B* **47**, 15500 (1993).
- [44] R. C. Jones, *J. Opt. Soc. Am.* **31**, 488 (1941).
- [45] M. S. Dresselhaus, G. Dresselhaus, and A. Jorio, *Group Theory* (Springer-Verlag, Berlin, 2008).
- [46] K. Ghalamkari, Y. Tatsumi, and R. Saito, *J. Phys. Soc. Jpn.* **87**, 024710 (2018).
- [47] Y. Tatsumi, T. Kaneko, and R. Saito, *Phys. Rev. B* **97**, 195444 (2018).
- [48] L. E. Golub and S. A. Tarasenko, *Phys. Rev. B* **90**, 201402(R) (2014).